frontiers in Materials

ORIGINAL RESEARCH
published: 28 January 2020
doi: 10.3389/fmats.2019.00348

Correlative Analysis of Specific Compatibilization in Composites by Coupling *in situ* X-Ray Scattering and Mechanical Tensile Testing

Britta Seidt[1,2], *Valeria Samsoninkova*[1,2,3], *Felix Hanßke*[3], *André Gjardy*[1], *Peter Fratzl*[1], *Hans G. Börner*[3] *and Wolfgang Wagermaier*[1]*

[1] Department of Biomaterials, Max Planck Institute of Colloids and Interfaces, Potsdam, Germany, [2] School of Analytical Sciences Adlershof, Humboldt-Universität zu Berlin, Berlin, Germany, [3] Laboratory for Organic Synthesis of Functional Systems, Department of Chemistry, Humboldt-Universität zu Berlin, Berlin, Germany

In this study, a bio-inspired hybrid material is investigated by *in situ* X-ray scattering experiments in combination with mechanical tensile testing. The material is composed of nanometer-sized spherical magnesium fluoride particles which are linked via material-specific peptide poly(ethylene glycol)-PEG conjugates to a semi-crystalline poly(ethylene oxide) PEO matrix. Mechanically relevant changes in crystal size and orientation in the PEO matrix are followed by wide angle X-ray scattering during the application of tensile stress. The amorphous phase of PEO is stabilized by the surface-engineered MgF_2 nanoparticles, leading to increased Young's modulus and tensile strength. Furthermore, small angle X-ray scattering experiments allowed the identification of a layer on the MgF_2 particle surfaces, which increases in thickness with the conjugate amount and leads to suppression of the agglomeration of MgF_2 nanoparticles. In conclusion, the use of selected peptide-PEG conjugates tailored to link MgF_2 particles to a PEO matrix successfully mimics the biological principle of interface polymers and suggests new directions for material fabrication for bio-applications.

Keywords: wide and small angle X-ray scattering, peptide-polymer conjugate, structure-function relationships, interface stabilization, functional material

OPEN ACCESS

Edited by:
Mario Guagliano, Politecnico di Milano, Italy

Reviewed by:
Leif Erik Asp, Chalmers University of Technology, Sweden
Hortense Le Ferrand, Nanyang Technological University, Singapore

***Correspondence:**
Wolfgang Wagermaier
wagermaier@mpikg.mpg.de

Specialty section:
This article was submitted to Polymeric and Composite Materials, a section of the journal Frontiers in Materials

Received: *14 August 2019*
Accepted: *31 December 2019*
Published: *28 January 2020*

Citation:
Seidt B, Samsoninkova V, Hanßke F, Gjardy A, Fratzl P, Börner HG and Wagermaier W (2020) Correlative Analysis of Specific Compatibilization in Composites by Coupling in situ X-Ray Scattering and Mechanical Tensile Testing. Front. Mater. 6:348. doi: 10.3389/fmats.2019.00348

INTRODUCTION

Inorganic fillers are widely used in synthetic polymers as well as in natural hybrid materials to enhance their mechanical performance. Especially biological hybrid materials, made of inorganic nanoparticles embedded in an organic matrix, are of great interest for material scientists in terms of their mechanical performance (Studart, 2012; Wegst et al., 2015). Bio-inspired hybrid materials with defined structuring of the material constituents across various length scales as well as precisely defined internal material interfaces exhibit advanced material properties (Bonderer et al., 2008; Munch et al., 2008; Studart, 2012; Wegst et al., 2015). Nature shows many examples of materials where the control over size, shape, and distribution of the composites' building blocks leads to hierarchically structured materials with outstanding mechanical properties. Bone is probably one of the most prominent examples of hierarchically structured hybrid materials with well-dispersed inorganic hydroxyapatite particles in a collagen matrix and tailored internal interfaces between these constituents (Fratzl et al., 2004b). The dominating influence of the nanostructure of hybrid

materials on their mechanical properties does not only depend on the properties of the individual components, but also on the interfaces between the components (Dujardin and Mann, 2002; Fratzl et al., 2004a; Meyers et al., 2008; Laaksonen et al., 2012). In Nature, the hydroxyapatite platelets in bone are bound to the collagen matrix by proteoglycans (Fratzl, 2003a; Fratzl et al., 2004a; Gupta et al., 2005) and the aragonite mineral crystals in nacre are linked by a series of proteins (Currey, 1977; Espinosa et al., 2009; Laaksonen et al., 2012). This concept of linking immiscible components by adding further polymer components to reduce the interfacial tension between phases is also used in hybrid materials science and usually termed as compatibilization (Kickelbick, 2003). The components are connected by thin layers of proteins that bind to the inorganic surfaces and compatibilize into the organic matrix to act as glue stabilizing the internal interfaces. The mineral phase in these materials provides strength, while the soft matrix allows ductility and toughness.

Research has been undertaken in recent years to develop new synthetic processing routes by applying design principles of Nature (Studart, 2012). One of the technical challenges during the embedding process of nanoparticles into the organic matrix is to avoid particle agglomeration to produce hybrid materials with homogeneously dispersed fillers. A large and diverse set of techniques is available in literature for the fabrication of bio-inspired hybrid materials, lasting from virus-based self-assembly to electrochemical deposition and sol-gel synthesis (Gregorczyk and Knez, 2016). Kemnitz et al. (2003) established a fluorolytic sol-gel synthesis for the preparation of nanoscopic metal fluorides with extraordinarily high specific surface areas. By using phosphonic acids to prevent agglomeration, Noack et al. (2011) utilized fluoride MgF_2 nanoparticles to prepare transparent organic-inorganic nanocomposites made of magnesium fluoride homogenously dispersed in organic polymers. MgF_2 has been shown to potentially being used in various biomedical applications, e.g., to coat the surface of biodegradable scaffolds for improved corrosion resistance and biological performance (Kang et al., 2016). Polymer composites consisting MgF_2 nanoparticles exhibit good biocompatibility and improved mechanical properties (Hansske et al., 2017).

In the last decades, few bio-inspired concepts were developed to tailor the interfaces between organic matrix and inorganic particles in synthetic hybrid materials (Palmer et al., 2008; Sommerdijk and de With, 2008; Hardy and Scheibel, 2010; Wang et al., 2011), e.g., by the use of material-affine peptide-PEG conjugates binding to the inorganic particles as well as anchoring the particles in the organic matrix (Hansske et al., 2015; Samsoninkova et al., 2017). By using a bio-combinatorial approach Hanßke et al. introduced specific stabilizers for sol-gel processes, which enable access to *de novo* modifying agents (Hansske et al., 2015). Twelve-mer peptides (comprised of 12 amino acids) have been selected from large peptide libraries covering a sequential space of $\sim 10^9$ different peptides. According to the adsorption behavior onto MgF_2 surfaces the most promising sequence was synthesized as a peptide-PEG conjugate (Hansske et al., 2015). The conjugates proved sequence-specific interactions with MgF_2 materials in a sol state, effectively stabilizing the sols in solution via surface modification and provided completely redispersible nanoparticles.

By using the peptide-PEG conjugates to stabilize and compatibilize MgF_2 nanoparticles in a PEO matrix Samsoninkova et al. prepared bio-inspired hybrid materials, which presented remarkable material properties in terms of stiffness and toughness (Samsoninkova et al., 2017). Increased Young's modulus (E) values and increased tensile toughness (R_m) values could be achieved. TEM showed an effective reduction of agglomeration and also influences on the form of the formed agglomerates by the presence of the peptide-PEG conjugates have been evident. SAXS measurements revealed sizes of primary particles to be in the range of 2–3 nm, while larger agglomerates of those were also present.

Within this study, structure-function relationship in model hybrid materials made of a PEO matrix and MgF_2 nanoparticles compatibilized by peptide-PEG conjugates were explored in view of material fabrication for bio-applications. The PEO matrix consists of (lamellar) crystalline and amorphous domains. The amounts of particles and conjugate were elucidated to optimize the mechanical performance of the hybrid materials. Multi-scale analysis tools were applied to perform simultaneous mechanical tensile testing and X-ray scattering experiments. By this approach, the role of unmodified nanoparticles, the use of the peptide-PEG conjugates alone and the combination of inorganic nanoparticles compatibilized by peptide-PEG conjugates in the PEO matrix in terms of the mechanical properties of the material were investigated. Changes in crystal orientation during applied tensile stress were followed to describe mechanically relevant reorientation effects of the crystalline domains. By examining the crystallite size and the deformation of the crystallites by recording the micro strain *in situ* on the crystallites, the crystalline as well as the amorphous phase were investigated.

EXPERIMENTAL SECTION

Sample Preparation

The hybrid materials were synthesized following a protocol described previously (Samsoninkova et al., 2017). In short, the surfaces of the spherical MgF_2 particles with a size of around 2–3 nm were non-covalently coated with a tailor-made peptide-PEG conjugate containing a monodisperse MgF_2-binding peptide sequence and a PEG block ($M_n = 3200\ g/mol$; GTQYYAYSTTQKS-*block*-PEG_{73}) to enhance the interactions with the PEO matrix material ($M_n = 900.000\ g/mol$) (Hansske et al., 2015). After solution blending in methanol, the hybrid materials were hot-pressed into thin hybrid films with a thickness of around 200 μm. Hot pressing of the hybrid materials was performed on a SPECAC device from Specac Limited (Orpington, UK) at a constant temperature of 70°C. First, the hybrid materials were heated without load for 3 min and then 1 ton of pressure was applied for 1 min, followed by 2 tons of pressure for 3 min. After cooling, samples were punched out with

Abbreviations: PEG, poly(ethylene glycol); PEO, poly(ethylene oxide); TEM, transmission electron microscopy; SAXS, small angle X-ray scattering; WAXS, wide angle X-ray scattering.

a bone-shaped stamp to match the tensile testing set-up. The sample compositions for the hybrid films were chosen with 15 wt.% MgF_2 and 0.5, 1.0, 2.0, 3.0, and 6.0 mol% conjugate, with non-filled PEO, PEO in combination with 3 mol% conjugate compatibilizer as well as PEO in combination with 15 wt.% MgF_2 fillers without the presence of compatibilizers as references.

X-Ray Scattering Experiments and Mechanical Tensile Testing

X-ray scattering experiments were performed at the synchrotron source BESSY II [Helmholtz-Zentrum Berlin für Materialien und Energie (HZB), Adlershof, Germany] at the μSpot beamline. Using a synchrotron source has the advantage that SAXS and WAXS measurements are possible simultaneously and a suitable time resolution is facilitated which is required for combined X-ray scattering and *in situ* tensile testing. X-ray patterns were recorded using an X-ray beam (100 μm in diameter; wavelength $\lambda = 0.82656$ Å) with a 2D CCD detector (MarMosaic 225, Rayonix Inc., Evanston, U.S.A.) with a pixel size of 73.242 μm and an array of 3,072 × 3,072 pixels. The calibrations of the sample-to-detector distance and beam center were performed using a quartz standard and analyzed with the software Fit2d (by Andy Hammersley, ESRF, v. 12.077). All patterns were corrected for empty beam background. Using the software packages DPDAK (Benecke et al., 2014) and OriginPro data evaluation was performed.

The crystallite sizes L of the polymer matrix were calculated by using the Scherrer equation:

$$L = \frac{k*\lambda}{C^*cos\,(\theta)}.$$

in which λ represents the wavelength, C the full width at half maximum of the (120) peak, θ the Bragg angle of the (120) peak and the Scherrer constant k (Holzwarth and Gibson, 2011). To correct the peak widths for instrumental broadening the measurements were performed using a Si111 monochromator with known instrumental contributions to C.

The tensile testing device was developed to perform simultaneous X-ray scattering experiments and mechanical tensile testing at a synchrotron source. A 20 N load cell (11E-020N-1a, Althen, Kelkheim, Germany) was used with a DC-encoder motor (M-126 DG, Physik Instrumente, Karlsruhe, Germany) to fit the requirements of the samples. To track the strain of the samples during tensile stress over the whole sample area and to perform video extensometry a camera (piA2400-17gm, pilot serie, Basler AG, Ahrensburg, Germany) with corresponding objective (TC 23 024, 2/3-Mpx detector, OPTO Engineering, Munich Germany) was used. **Figure 1** shows the schematic design of the *in-situ* tensile testing set-up and two halves of typical x-ray scattering patterns for 0 and 50% strain.

To measure Young's modulus E and nominal tensile strength R_m stress-strain curves were recorded ($E = \frac{\sigma}{\varepsilon}$), where σ represents the recorded stress and ε the recorded strain, to the linear-elastic region between 1 and 3% strain of the recorded stress-strain curve Young's modulus values were achieved. The macro strain ε was obtained by video extensometry using a camera observing the elongation Δl of the distance l_0 between black markers on the sample ($\varepsilon = \Delta l/l_0$). As reported earlier (Samsoninkova et al., 2017), samples exhibit different values for elongation at break, depending on the amount of conjugate, ranging from around 700 up to 900%. A limitation of our study is, that the used synchrotron *in-situ* tensile tester did not allow elongating up to such high deformations.

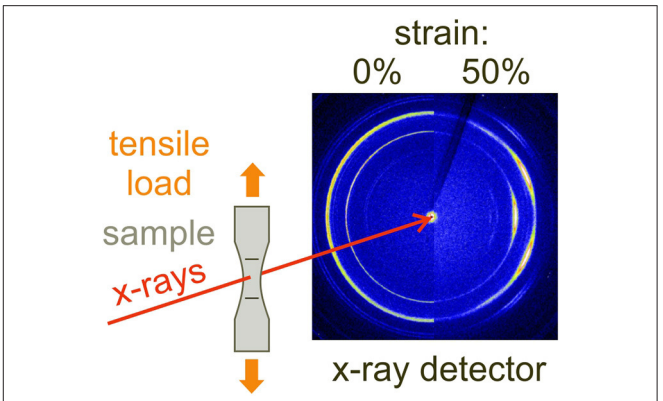

FIGURE 1 | Experimental *in-situ* X-ray scattering setup combined with mechanical tensile testing. Tensile load is applied to the sample, which is simultaneously scanned by an X-ray beam. Two-dimensional X-ray diffraction patterns are recorded by a two-dimensional detector (shown: two halves of diffraction patterns representing 0 and 50% strain).

Molecular deformations induced by applied tensile stress within polymers leads to a micro strain in crystallites and causes a peak shift of the crystalline X-ray diffraction peaks (Mallick et al., 2006). By applying the following equation to the X-ray scattering data the micro strain ε_{micro} could be calculated:

$$\varepsilon_{micro} = \frac{q_0 - q_\varepsilon}{q_\varepsilon}$$

with q_0 as the q value of the (120) signal position before applied tensile stress and q_ε as the q value after applied tensile stress.

RESULTS

In this study, a combination of mechanical tensile testing in combination with SAXS and WAXS was used to provide insights into structure-function relationships. By performing SAXS experiments, the size and shape as well as the agglomeration behavior of the MgF_2 nanoparticles were investigated. *In situ* WAXS experiments combining X-ray scattering and mechanical tensile testing allowed a detailed analysis of the relationship between structure and mechanical properties of the hybrid material by examining the crystallite size and deformation of the crystallites during applied tensile stress of the matrix material PEO.

Size and Arrangement of the Incorporated Nanoparticles

The radius of the MgF_2 particles R (Samsoninkova et al., 2017), as well as the fractal dimension D was determined by applying

the following equation described in Samsoninkova et al. (2017) on the SAXS data.

$$I(q) = I_0 B + I_0 \left[V_0 S(q) P(q) \right]$$

For calculating the true layer thickness (δ) of the conjugate layer coating the MgF_2 particles the following equation was used to relate the differences of the electron densities of MgF_2 with $\rho(r) = 0.91\ e^{-1}/\text{Å}^3$, $\rho(r) = 0.38\ e^{-1}/\text{Å}^3$ for PEO (Glatter et al., 1994) and $\rho(r) = 0.45\ e^{-1}/\text{Å}^3$ for the conjugate by using the biomolecular scattering length density calculator (http://psldc.isis.rl.ac.uk/Psldc/).

$$R^2 = \frac{(R_P + \delta)^5 C_K + R_P^5 (C_P - C_K)}{(R_P + \delta)^3 C_K + R_P^3 (C_P - C_K)}$$

The electron density difference between PEO and MgF_2 is defined as C_P, while C_K is the electron density difference between PEO and conjugate. The radius of the primary particles is defined as R, while R_P gives the particle radius in combination with peptide-PEG conjugates revealed by SAXS experiments (Samsoninkova et al., 2017). Therefore, the equation can be converted into the corrected layer thickness to calculate the increasing particle radius due to adhesion of the conjugate to the MgF_2 nanoparticle surface. **Table 1** shows the calculated values for the true layer thickness δ of different sample compositions. The dependency of δ on the conjugate amount is displayed in **Figure 2A**. Looking at the dependency of conjugate amount**,** up to 1.0 mol% conjugate a slight increase, followed by a strong increase starting at 2.0 mol% conjugate can be observed with a slow further increase.

Furthermore, by calculating the fractal dimension D the morphology and the state of agglomeration can be investigated. It can be seen as a value for the degree of branching within the structure of a material (Logan and Kilps, 1995; Husing et al., 1998; Bushell et al., 2002; Fratzl, 2003b). Lower values for D in aggregates refer to less branching, while higher values represent higher branching and therefore, more densely packed agglomerates (Emmerling et al., 1995; Logan and Kilps, 1995; Husing et al., 1998; Bushell et al., 2002). By plotting the fractal dimension D *vs.* used mol% conjugate a dependency of the agglomeration behavior and amount of used conjugate could be observed. Up to 1.0 mol% conjugate, the values for the fractal dimension D did not differ significantly and were maintained in a range between D = 1.74-1.77. At 2.0 mol% conjugate a significant decrease to around D = 1.47 can be observed with a slow further decrease. The dependency of the fractal dimension D and the used conjugate ratio is shown in **Figure 2B**, which indicates an inverse behavior for the fractal dimension D compared to the true layer thickness δ. Both graphs exhibit strong changes between 1.0 and 2.0 mol% conjugate.

In situ Tensile Testing

The samples were measured at the μSpot beamline at BESSY II to perform simultaneous tensile testing and X-ray scattering experiments. With the recorded stress-strain curves every sample could be investigated for Young's modulus E and nominal tensile strength R_m (based on the original cross section area). **Figure 3** shows an exemplary stress-strain curve of non-filled PEO as reference to demonstrate the origin of the determined values for Young's modulus E and tensile strength R_m.

The measurements were interrupted to record WAXS patterns at 0, 1, 3, 5, 8, 10, 20, 30, 50% strain. These stops occurred as an area with decreasing stress in the stress-strain curves during constant strain. At every stop, 10 diffraction patterns were recorded to ensure measurements in the deformation area of the hybrid material. As the areas where necking occurred in the samples were hard to predict, 10 points with a distance of 300 μm were measured in longitudinal direction of the sample. **Table 2** shows the Young's moduli and the tensile strengths of the samples.

With the insertion of MgF_2 nanoparticles and conjugate the values for both determined material parameters increased. The values for Young's modulus increased by nearly factor 2 after MgF_2 incorporation and even more after addition of

TABLE 1 | Results for conjugate layer thickness δ and fractal dimension D.

Sample	δ (nm)	D
PEO + 15 wt.% MgF_2 + 0.5 mol% conjugate	2.9	1.77 ± 0.02
PEO + 15 wt.% MgF_2 + 1.0 mol% conjugate	3.7	1.74 ± 0.03
PEO + 15 wt.% MgF_2 + 2.0 mol% conjugate	6.4	1.47 ± 0.04
PEO + 15 wt.% MgF_2 + 3.0 mol% conjugate	6.6	1.47 ± 0.09
PEO + 15 wt.% MgF_2 + 6.0 mol% conjugate	7.4	1.44 ± 0.02

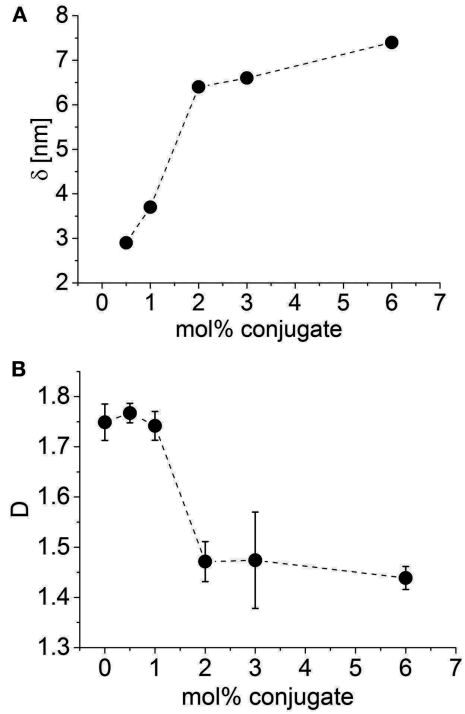

FIGURE 2 | Dependency of **(A)** true layer thickness δ and **(B)** fractal dimension D on amount of added conjugate in the composition. Both curves show strong changes between 1.0 and 2.0 mol% conjugate.

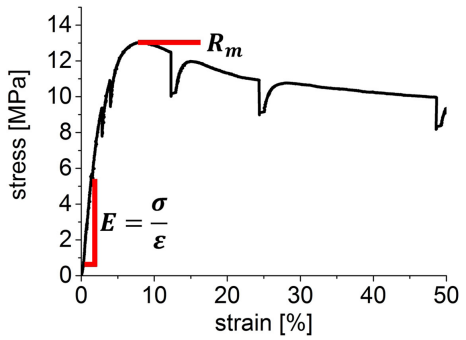

FIGURE 3 | Representative stress-strain curve of non-filled PEO with characteristic parameters marked on the graph showing the mechanical material properties by tensile strength R_m and Young's modulus E. The drops in stress during constant tensile strain result from required stops during the measurements necessary to record X-ray diffraction patterns with larger accuracy.

TABLE 2 | Young's moduli and tensile strengths of *in situ* mechanical tensile testing experiments.

Sample	E (MPa)	R_m (MPa)
Non-filled PEO	330 ± 75	11.8 ± 0.9
PEO +0 wt.% MgF_2 + 3.0 mol% conjugate	374 ± 125	10.5 ± 1.1
PEO + 15 wt.% MgF_2 + 0 mol% conjugate	583 ± 30	12.9 ± 1.0
PEO + 15 wt.% MgF_2 + 2.0 mol% conjugate	592 ± 183	12.2± 0.7
PEO + 15 wt.% MgF_2 + 3.0 mol% conjugate	766 ± 202	12.0 ± 0.6
PEO + 15 wt.% MgF_2 + 6.0 mol% conjugate	890 ± 53	14.7 ± 1.2

conjugate. Also tensile strengths increased with MgF_2 and conjugate insertion. The sample composition with 6.0 mol% conjugate showed the highest values for Young's modulus and tensile strength.

In situ Wide Angle X-Ray Diffraction Studies

The commonly observed WAXS patterns of semi-crystalline PEO samples describe a monoclinic lattice (Zhu et al., 2000). Based on this, several reflections in the reciprocal space could be seen, which were coexistent with the experimental WAXS data. Two prominent signals could be obtained in the WAXS signal with $q = 13.6\ nm^{-1}$ and $q = 16.4\ nm^{-1}$. The first signal corresponds to the reflection of the (120) plane lying perpendicular to the *c*-axis of the crystallites (crystalline domains). The second signal corresponds to the reflections of overlapping rings from the (032), ($\bar{1}$32), ($\bar{2}$12), (112), ($\bar{1}$24), ($\bar{2}$04), and (004) planes, which are hard to distinguish and therefore, not used for further analysis (Zhu et al., 2000; Lai et al., 2012).

At 50% strain, a clear texture of both signals was observed. **Figure 4** shows two-dimensional diffraction patterns of non-filled PEO (**Figure 4A**) before tensile testing and (**Figure 4B**) at 50% tensile strain during applied tensile stress. The (120) plane, which was used for further data evaluation showed a strong meridional texture after applied tensile stress. The (120) reflection has an angle of 90° to the *c*-axis in PEO crystals. Different integration angles were chosen for the two-dimensional data processing of the (120) signal to consider the differences of the crystallites according to the orientation of the *c*-axis during the applied tensile stress. This enables an interpretation of the progression of crystallite orientations during deformation. The angles were selected perpendicular to the tensile direction and directly in tensile direction with an angle of 30°. The defined integration areas are shown in **Figures 4A,B** with corresponding one-dimensional radial profiles where the *c*-axis crystallite orientation is aligned (**Figure 4C**) in tensile direction and (**Figure 4D**) perpendicular to the tensile direction.

Two effects on the radial profiles could be observed depending on the *c*-axis crystallite orientation. They show obvious differences in the peak broadening and the positions of the (120) signal. Perpendicular to the tensile direction, a peak broadening after applied tensile stress is visible, whereas in tensile direction broadening appeared with much less intensity. Additionally, the peak positions before tensile testing and at 50% strain with different integration areas differ greatly. Perpendicular to the tensile direction no peak shifting could be observed, whereas in tensile direction a peak shift to lower q values appeared. These two effects on the (120) signal were evaluated to gain information about the crystalline and the amorphous phases. By quantifying the peak broadening of the signal it was possible to measure the average crystallite size (Holzwarth and Gibson, 2011) within the crystalline lamellae and hence, to make statements about the crystallite perfection of the crystalline phase. The crystallite size as well as the determined micro strain during applied tensile stress can be plotted against the applied macro strain to reveal information about structure-function relationships on both the micro and nanometer scale. In **Figure 5**, the crystallite size vs. the macro strain is drawn (**Figure 5A**) with the *c*-axis crystallite orientation in and (**Figure 5B**) perpendicular to the tensile direction, as well as the micro strain vs. the macro strain with (**Figure 5C**) the *c*-axis crystallite orientation in and (**Figure 5D**) perpendicular to the tensile direction. Evaluating the crystallite sizes with *c*-axis crystallite orientation in tensile direction, after the insertion of conjugate and MgF_2 nanoparticles a decrease of the crystallite sizes could be observed. With increasing macro strain the crystallite sizes strongly decreased for all investigated samples down to sizes of $L = 10 - 20\ nm$. The same applied for the crystallite sizes with the *c*-axis crystallite orientation perpendicular to the tensile direction but only down to sizes of $L = 30 - 40\ nm$, as the crystallites are getting aligned during applied tensile stress in tensile direction. For this reason, we focused on the crystallite sizes with *c*-axis crystallite orientation in tensile direction for further data evaluation.

By comparing the induced micro strain on the crystalline domains in PEO vs. macro strain a different behavior could be seen for the *c*-axis crystallite orientations. With a *c*-axis crystallite orientation (**Figure 5C**) in tensile direction negative values for micro strain appeared, whereas the crystallites oriented (**Figure 5D**) perpendicular to the tensile direction showed a strong increase of the micro strain, with increasing macro strain up to a plateau where the values reached a constant level.

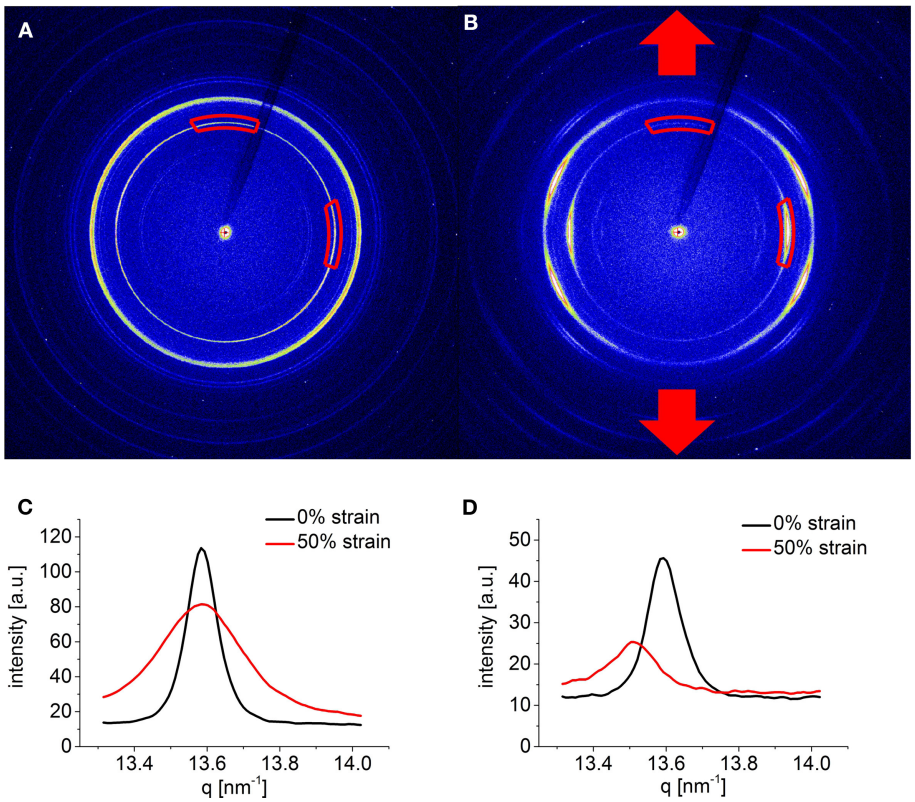

FIGURE 4 | Two-dimensional diffraction patterns of non-filled PEO **(A)** before and **(B)** at 50% tensile strain. Before applied tensile stress, only weak textures as a result of sample preparation were visible in the Debye Scherrer rings, whereas the rings at 50% strain show a distinct texture. **(C)** Radial profiles before and at 50% tensile strain of the (120) signal with a c-axis crystallite orientation in tensile direction. A broadening of the signal appeared at 50% tensile strain. **(D)** Radial profiles before and at 50% tensile strain of the (120) signal with a c-axis crystallite orientation perpendicular to the tensile direction. A peak shift to lower q values appeared after applied tensile stress.

For further data interpretation and to compare the samples between themselves the percentage crystallite size change (CSC) was drawn *vs.* macro strain and the slope within the elastic range between 1 and 3% strain was determined (**Figure 6A**). The mean values and corresponding standard deviations were drawn as bar charts in **Figure 6B** for $n = 3$ samples. The insertion of the conjugate led to a strong decrease of the slope of the percentage CSC within the elastic range, whereas the insertion of MgF_2 in combination with conjugate led to an increase of the slope up to a factor 2. This means that only the insertion of MgF_2 nanoparticles compatibilized by the peptide-PEG conjugate caused faster decreasing crystallite sizes under load.

The slope of the micro strain *vs.* macro strain of the crystallites with the *c*-axis oriented perpendicular to the tensile direction was determined within the elastic regime (**Figure 6C**). Allowing statements on the force transmission from the amorphous to the crystalline phase of the organic semi crystalline matrix. This is a key point to explain materials mechanical properties. All values were drawn as bar charts for $n = 3$ samples in **Figure 6D** with corresponding standard deviations. By using compatibilized MgF_2 nanoparticles higher values of the slope up to a factor of 4 could be realized, whereas the plateau values (**Figure 6E**) stayed almost in the same range for all sample compositions of the stabilized composites. This means that the transmitted force from the amorphous to crystalline phase was the same for all sample compositions, but the force transmission from the amorphous to the crystalline phase occurred earlier after MgF_2 nanoparticle compatibilization.

DISCUSSION

In this study, relations between nano-structure and deformation mechanisms at several length scales in a new hybrid material consisting of PEO as a semi-crystalline polymer matrix and MgF_2 nanoparticles was investigated. By using an MgF_2-affine peptide-PEG conjugate, the nanoparticles were compatibilized in the PEO matrix and the function of interface polymers as found in natural hybrid materials could be mimicked.

The samples were investigated for layer thickness of the conjugate δ and fractal dimension D by performing small angle X-ray scattering experiments. Recently, a study with congeneric PEO/MgF_2 hybrid materials revealed decreasing agglomerate sizes on increased conjugate amounts (Samsoninkova et al., 2017). In the present system, this effect was explained by

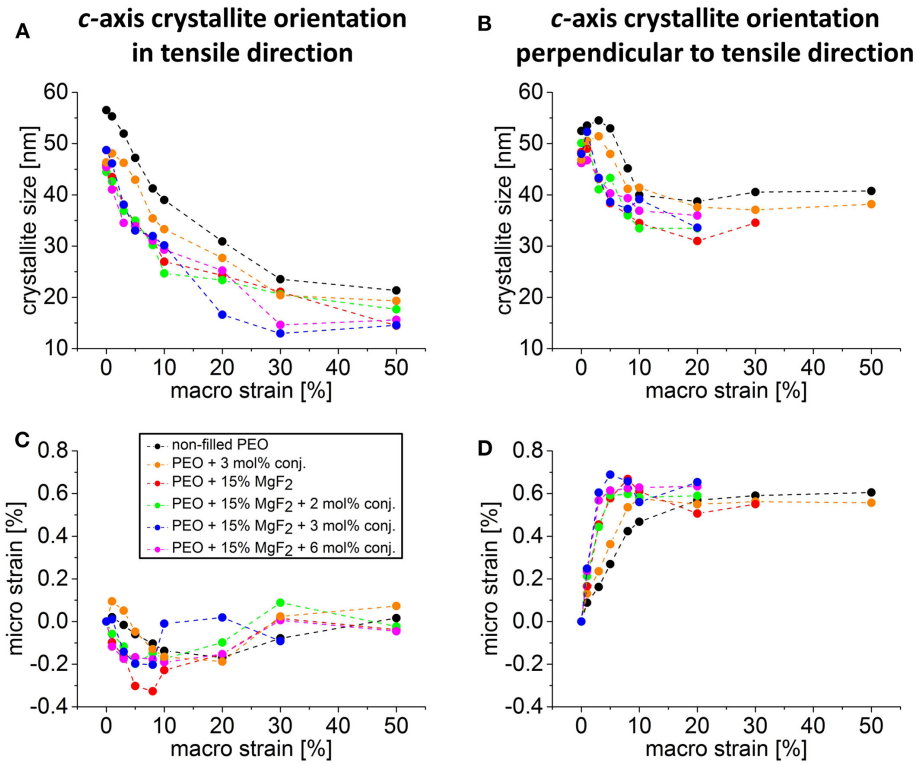

FIGURE 5 | Plots of crystallite sizes *vs.* macro strain with c-axis crystallite orientation **(A)** in and **(B)** perpendicular to the tensile direction of exemplary sample compositions. The crystallite size changes to lower sizes after MgF_2 and conjugate insertion and with increasing macro strain. Major changes of the crystallite sizes can be seen with increasing macro strain with the c-axis crystallite orientation in tensile direction. The applied micro vs. macro strain is drawn with the c-axis crystallite orientation **(C)** in tensile direction and **(D)** perpendicular to the tensile direction. With increasing macro strain the micro strain showed negative values for the c-axis crystallite orientation in tensile direction and increasing positive values up to a plateau perpendicular to the tensile direction. Dotted lines in the graph are shown to aid the eye.

the thickness of the conjugate layer on the MgF_2 surface, which was found to increase with the amount of conjugate. Based on the differences in electron density of the different components, the layer thickness was calculated. From these results, a saturation of the MgF_2 surface at 2 mol% conjugate with a layer thickness of $\delta = 6.4\ nm$ was concluded, because at this composition the system showed an abrupt change in δ. This conclusion was confirmed by calculating the fractal dimension D as a value for the degree of branching within the system (Schmidt, 1991; Peterlik and Fratzl, 2006). The abrupt change between 1.0 and 2.0 mol% for the fractal dimension D can be interpreted as the transition to more open fractal structures leading to a suppression of agglomeration. The effect of the addition of stabilizing agents to nanoparticles by binding to the particle surfaces was described in different studies as a prevention of uncontrolled growth and aggregation (Niemeyer, 2001), which can be also confirmed in this study. The interpretation of the SAXS results is schematically illustrated in **Figure 7A**. With increasing conjugate amount an increasing layer of conjugate around MgF_2 particles is found as well as reduced agglomeration of the particles. The investigated hybrid materials with higher conjugate amount showed less branched particle networks.

Improved mechanical properties were found with higher conjugate amounts, leading to increased Young's moduli and tensile strengths. The sample set with 15 wt.% MgF_2 stabilized by 6.0 mol% conjugate exhibited obviously the highest reinforcement effect. The Young's moduli of these compatibilized hybrid materials were increased almost by a factor of 2 compared to non-stabilized composites. This confirms prior observations that the amount of compatibilizers has to reach about 3.0–6.0 mol% to provide materials interface stabilization effectively (Samsoninkova et al., 2017). There, samples showed values for elongation at break from around 730% (15 wt.% MgF_2 and 0 mol% conjugate), a relative maximum of around 930% (15 wt.% MgF_2 and 1 mol% conjugate) to around 690% (15 wt.% MgF_2 and 3 mol% conjugate), while samples with 15 wt.% MgF_2 and 6 mol% conjugate showed a strong reduction in ductility and therefore only around 70% elongation at break. Therefore, an amount of around 1–3 mol% conjugate seems to give an optimal compromise to achieve relatively high stiffness and toughness in these hybrid materials with 15 wt.% MgF_2 nanoparticles.

By performing WAXS experiments two prominent peaks were identified as characteristic PEO signals corresponding to the (120) plane at $q = 13.6\ nm^{-1}$ and an overlay of different rings from the $(\bar{1}32)$, $(\bar{2}12)$, (032), (004), $(\bar{2}04)$, and $(\bar{1}24)$

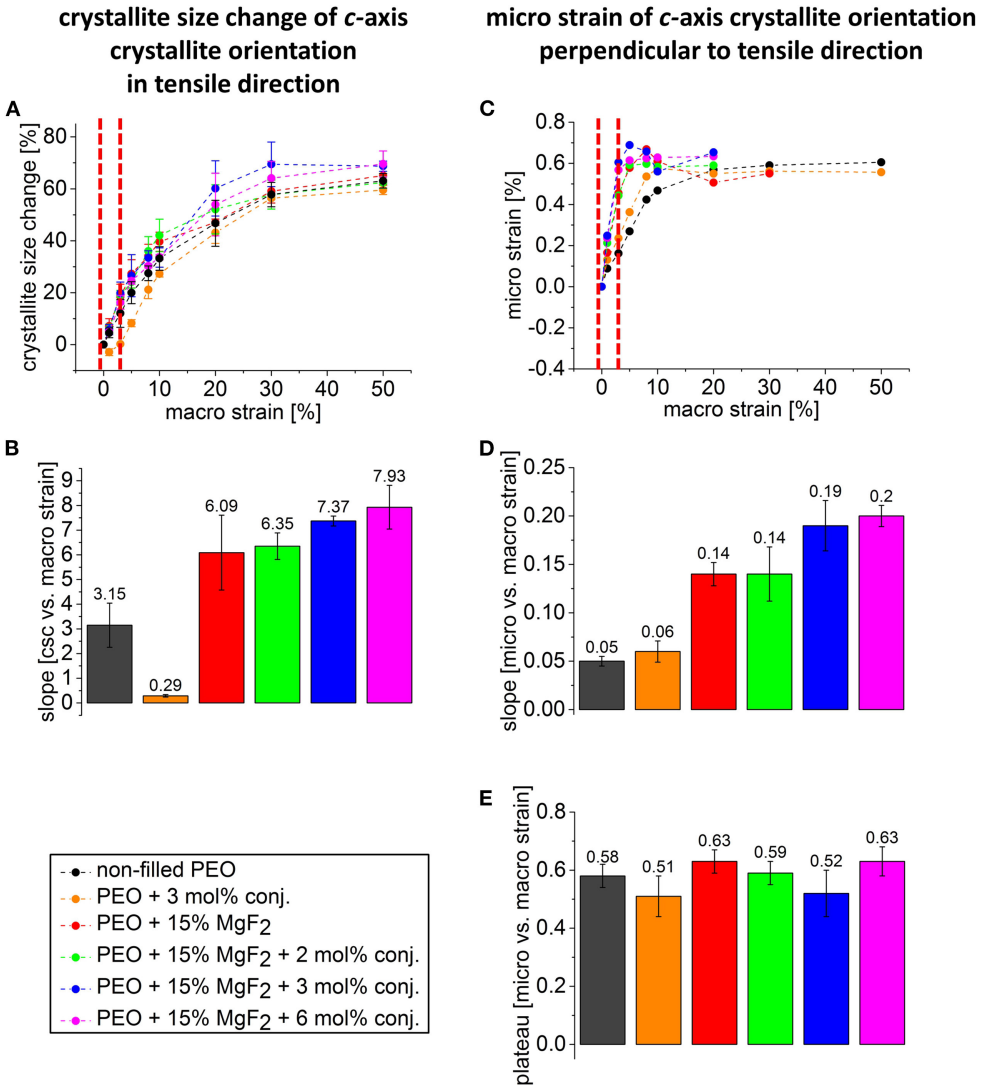

FIGURE 6 | Percentage crystallite size change **(A)** of the crystallites with the c-axis aligned in tensile direction. The slope was determined within the elastic range (red bars) and drawn as bar charts **(B)** with corresponding standard deviation for $n = 3$ samples. An increase of the values can be observed after the insertion of MgF_2 compatibilized by the peptide-PEG conjugate and therefore, a faster decrease of the crystallite sizes during applied tensile stress. Also the slope of micro *vs.* macro strain **(C)** within the elastic range (red bars) of the crystallites with the c-axis aligned perpendicular to the tensile direction was determined. The results were drawn as bar charts **(D)** as well as the plateau values **(E)** for $n = 3$ samples. Again an increase after insertion of compatibilized MgF_2 could be observed for the slope values, whereas the plateau values stayed in the same range for all sample compositions.

planes. During applied tensile stress a clear texture of both rings appeared in the two-dimensional WAXS pattern. The (120) signal showed two strong meridional arcs with increasing tensile strain. By comparing the WAXS patterns at 50% strain with simulated 2D WAXS patterns from literature, we could assume that during applied tensile stress the (120) plane, which lies perpendicular to the *c*-axis, is meridional aligned to the tensile direction. Therefore, the *c*-axis is becoming aligned in tensile direction (Adams et al., 1986; Petermann and Ebener, 1999; Zhu et al., 2000; Lai et al., 2012). Due to the crystalline structure of PEO with an angle of 90° between the (120) plane and the *c*-axis, this correlation can be used to make predictions about the crystalline structure by examining the peak broadening and position during applied tensile stress.

The crystallite size changes were evaluated by calculating the crystallite sizes of the (120) plane. By performing the two mentioned integration areas the crystallite size change during applied tensile stress of the crystalline phase aligned in tensile direction was described. The (120) plane lies perpendicular to the *c*-axis and is meridional aligned during applied tensile stress. This fact gives the possibility to make direct conclusions about the crystalline phase and correlate them with material properties. The determined slope of the percentage crystallite size change vs. macro strain, allows the making of statements

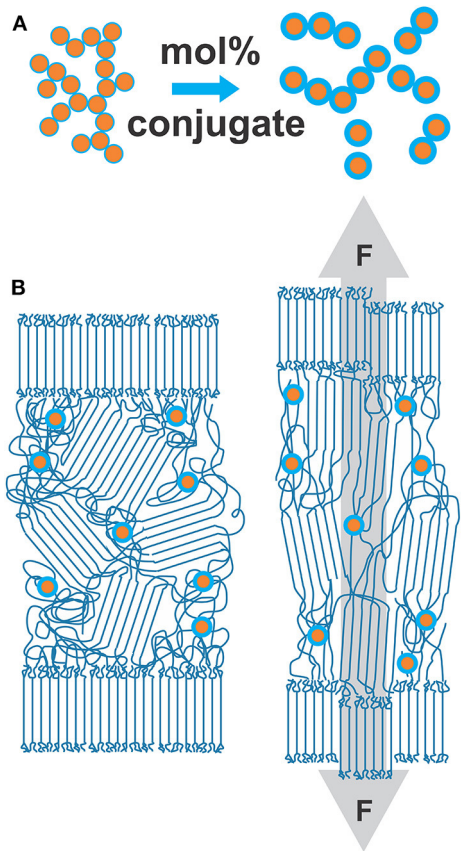

FIGURE 7 | Schematic representation of the hybrid material at the nanometer scale. **(A)** Increasing amount of conjugate leads to higher layer thickness and reduces agglomeration (less branched aggregates) as derived from the fractal dimension D. **(B)** Deformation mechanisms of PEO + 15 wt.% conjugated MgF_2 during applied tensile stress. The use of conjugate led to a stabilization of the amorphous phase. The stabilization of MgF_2 nanoparticles by the peptide-PEG conjugate blocked the movement of dislocations within the amorphous phase. The amorphous PEO chains cannot elongate as in non-filled PEO and the force transmission from the amorphous to the crystalline phase appears earlier resulting in a faster block-slip mechanisms and therefore, decreasing crystallite sizes.

concerning the deformation mechanism of the hybrid material. As reference, non-filled PEO was measured with a value of $m = 3.15$, whereas the reference sample of non-filled PEO in combination with compatibilized MgF_2 showed a clear decrease in the slope. This flatter slope can be explained by a softening of the amorphous phase. With a factor of 2, an increase of $m = 6.1$ could be seen after MgF_2 insertion with increasing values for increasing conjugate amounts. This increase can be rationalized probably by a positive effect of the compatibilized MgF_2 nanoparticles on the amorphous phase of the matrix. Comparable to the interface polymers in natural materials, the PEG-blocks adsorption on surfaces of compatibilized MgF_2 particles enhanced apparently the interactions with the PEO matrix, leading to a better mechanical performance of the interface-engineered hybrid materials. This effect is even improved by the use of higher equivalents of the peptide-PEG conjugate.

Additional information could be gained by calculating the micro strain within the crystalline domains. Firstly, the negative values of the strain aligned in tensile direction could be explained by reasonable Poisson ratio values of around $\mu = 0.3$. The Poisson ratio describes the relation between longitudinal to lateral deformation during tensile stress and the most common materials such as polymers or composites hold a Poisson ratio of $0.25 < \mu < 0.35$ (Askeland et al., 2010; Rawlings et al., 2013; Silberschmidt and Matveenko, 2015). These values fit well to the determined values and appoints to an increase of the volume during applied tensile stress, since materials with a Poisson ratio $\mu > 0.5$ show a decrease of the volume during applied tensile stress.

The process of deformation for bulk semi-crystalline polymers has been described by different studies (Adams et al., 1986; Petermann and Ebener, 1999; Zhu et al., 2000; Liu et al., 2006). The deformation in such materials during applied tensile load can be characterized by an initial elongation of the amorphous phase, followed by a shearing and tilting of the lamellar folded chains. Afterwards, block crystals are pulled out of the lamellae, which is referred to as "block slip" mechanism and those blocks become further aligned along the tensile axis (Adams et al., 1986; Petermann and Ebener, 1999; Lai et al., 2012).

Statements about the force transmission from the amorphous to the crystalline phase could be made by determining the slope of the micro vs. the macro strain of the crystallites aligned perpendicular to the tensile direction. Higher values indicate a faster force transmission from the amorphous to the crystalline phase, as it is known that deformation of semi-crystalline block polymers starts with an elongation of the amorphous phase. After insertion of MgF_2 compatibilized by the conjugate the energy transmission appeared faster with a factor of 4. This increase can be explained by the increased interactions between the filler particles and the polymer matrix, which resulted in a stabilization of the amorphous phase. As reported earlier (Samsoninkova et al., 2018), the MgF_2 particles are non-covalently coated with peptide-PEG conjugates and by means of NMR study we found mixtures of interactions but predominantly electrostatic ones. By applying uniaxial tensile stress on the hybrid material initially, the statistical coil conformation of the PEO chains in the amorphous phase were extended and aligned. This process is apparently modulated by the compatibilized MgF_2 filler that were anchored in the PEO matrix and thus leading as physically network points to a more efficient force transmission in the hybrid material. This accelerated pull out of the lamellae and decreasing crystallite sizes proved the block slip mechanism. The main findings of the *in situ* X-ray scattering experiments for the stabilized hybrid material are illustrated in **Figure 7B**. By stabilizing the MgF_2 particles with the conjugate the amorphous phase is becoming stabilized and therefore, the force transmission from the amorphous to the crystalline phase appeared earlier resulting in higher slopes for micro *vs.* macro strain and decreasing crystallite sizes. Samples with higher conjugate amount and less branched particle networks might also exhibit a reorientation of

these branches; most likely an alignment of single branches along the loading directions.

CONCLUSIONS

A detailed study on the deformation mechanism in PEO/MgF_2 hybrid materials in the presence of specific compatibilizers was performed by the use of *in situ* X-ray scattering experiments and tensile testing. By evaluating the crystallite size change and the micro strain of the crystallites a stabilization of the amorphous phase followed by a more efficient force transmission from the amorphous to the crystalline phase could be proven by the combination of MgF_2 nanoparticles compatibilized by the MgF_2-binding peptide-PEG conjugate. The concept of tailor-made bio-inspired interfaces by the use of material-specific peptide-PEG conjugates was verified as a new route to prepare synthetic hybrid materials with enhanced mechanical properties. By mimicking aspects of interfacial proteins from biomaterials the peptide-PEG conjugates proved to act as interfacial "glue" and improved the tensile strength and Young's modulus in comparison to non-stabilized composite materials. This study provides new insights into possible approaches toward a new class of bio-inspired hybrid materials with tailored interface chemistry. By this approach, it might be possible to fabricate materials with similar structure-function relations as found in natural hybrid materials and making them therefore good candidates for bio-applications.

DATA AVAILABILITY STATEMENT

All datasets generated for this study are included in the article/supplementary material.

AUTHOR CONTRIBUTIONS

Samples have been prepared by VS and FH. Experiments have been performed by BS, AG, and WW. Data evaluation has been done by BS and AG. The manuscript has been written through contributions of all authors. All authors have given approval to the final version of the manuscript.

FUNDING

We acknowledge financial support from the German Research Council in a frame of the excellence initiative at Graduate School of Analytical Sciences Adlershof (SALSA). HB acknowledges in addition the European Research Council under the European Union's 7th Framework Program (FP07-13)/ERC Starting grant Specifically Interacting Polymer–SIP (ERC 305064).

ACKNOWLEDGMENTS

We would like to thank Dr. Chenghao Li (μSpot beamline), Dr. Stefan Siegel (μSpot beamline), Petra Leibner (MPI-KG), and Gunthard Benecke for technical support.

REFERENCES

Adams, W. W., Yang, D., and Thomas, E. L. (1986). Direct visualization of microstructural deformation processes in polyethylene. *J. Mater. Sci.* 21, 2239–2253. doi: 10.1007/BF01114262

Askeland, D., Fulay, P., and Wright, W. (2010). *The Science and Engineering of Materials.* Cengage Learning.

Benecke, G., Wagermaier, W., Li, C. H., Schwartzkopf, M., Flucke, G., Hoerth, R., et al. (2014). A customizable software for fast reduction and analysis of large X-ray scattering data sets: applications of the new DPDAK package to small-angle X-ray scattering and grazing-incidence small-angle X-ray scattering. *J. Appl. Crystallogr.* 47, 1797–1803. doi: 10.1107/S1600576714019773

Bonderer, L. J., Studart, A. R., and Gauckler, L. J. (2008). Bioinspired design and assembly of platelet reinforced polymer films. *Science* 319, 1069–1073. doi: 10.1126/science.1148726

Bushell, G., Yan, Y., Woodfield, D., Raper, J., and Amal, R. (2002). On techniques for the measurement of the mass fractal dimension of aggregates. *Adv. Colloid Interface Sci.* 95, 1–50. doi: 10.1016/S0001-8686(00)00078-6

Currey, J. D. (1977). Mechanical properties of mother of pearl in tension. *Proc. R. Soc. Lond. B: Biol. Sci.* 196, 443–463. doi: 10.1098/rspb.1977.0050

Dujardin, E., and Mann, S. (2002). Bio-inspired materials chemistry. *Adv. Mater.* 14, 775–788. doi: 10.1002/1527-2648(20020717)4:73.0.CO;2-K

Emmerling, A., Petricevic, R., Beck, A., Wang, P., Scheller, H., and Fricke, J. (1995). Relationship between optical transparency and nanostructural features of silica aerogels. *J. Non-Cryst. Solids* 185, 240–248. doi: 10.1016/0022-3093(95)00021-6

Espinosa, H. D., Rim, J. E., Barthelat, F., and Buehler, M. J. (2009). Merger of structure and material in nacre and bone – perspectives on de novo biomimetic materials. *Prog. Mater. Sci.* 54, 1059–1100. doi: 10.1016/j.pmatsci.2009.05.001

Fratzl, P. (2003a). Cellulose and collagen: from fibres to tissues. *Curr. Opin. Colloid Interface Sci.* 8, 32–39. doi: 10.1016/S1359-0294(03)00011-6

Fratzl, P. (2003b). Small-angle scattering in materials science - a short review of applications in alloys, ceramics and composite materials. *J. Appl. Crystallogr.* 36, 397–404. doi: 10.1107/S0021889803000335

Fratzl, P., Burgert, I., and Gupta, H. S. (2004a). On the role of interface polymers for the mechanics of natural polymeric composites. *Phys. Chem. Chem. Phys.* 6, 5575–5579. doi: 10.1039/b411986j

Fratzl, P., Gupta, H. S., Paschalis, E. P., and Roschger, P. (2004b). Structure and mechanical quality of the collagen-mineral nano-composite in bone. *J. Mater. Chem.* 14, 2115–2123. doi: 10.1039/B402005G

Glatter, O., Scherf, G., Schillen, K., and Brown, W. (1994). Characterization of a poly (ethylene oxide)-poly (propylene oxide) triblock copolymer (EO27-PO39-EO27) in aqueous solution. *Macromolecules* 27, 6046–6054. doi: 10.1021/ma00099a017

Gregorczyk, K., and Knez, M. (2016). Hybrid nanomaterials through molecular and atomic layer deposition: top down, bottom up, and in-between approaches to new materials. *Prog. Mater. Sci.* 75, 1–37. doi: 10.1016/j.pmatsci.2015.06.004

Gupta, H. S., Wagermaier, W., Zickler, G. A., Raz-Ben Aroush, D., Funari, S. S., et al. (2005). Nanoscale deformation mechanisms in bone. *Nano Lett.* 5, 2108–2111. doi: 10.1021/nl051584b

Hanssske, F., Bas, O., Vaquette, C., Hochleitner, G., Groll, J., Kemnitz, E., et al. (2017). Via precise interface engineering towards bioinspired composites with improved 3D printing processability and mechanical properties. *J. Mater. Chem. B* 5, 5037–5047. doi: 10.1039/C7TB00165G

Hanssske, F., Kemnitz, E., and Borner, H. G. (2015). Generic biocombinatorial strategy to select tailor-made stabilizers for sol-gel nanoparticle synthesis. *Small* 11, 4303–4308. doi: 10.1002/smll.201500162

Hardy, J. G., and Scheibel, T. R. (2010). Composite materials based on silk proteins. *Prog. Polym. Sci.* 35, 1093–1115. doi: 10.1016/j.progpolymsci.2010.04.005

Holzwarth, U., and Gibson, N. (2011). The Scherrer equation versus the 'Debye-Scherrer equation'. *Nat Nano* 6, 534–534. doi: 10.1038/nnano.2011.145

Husing, N., Schubert, U., Misof, K., and Fratzl, P. (1998). Formation and structure of porous gel networks from Si(OMe)(4) in the presence of

A(CH2)(n)Si(OR)(3) (A = functional group). *Chem. Mater.* 10, 3024–3032. doi: 10.1021/cm980706g

Kang, M. H., Jang, T. S., Kim, S. W., Park, H. S., Song, J., Kim, H. E., et al. (2016). MgF2-coated porous magnesium/alumina scaffolds with improved strength, corrosion resistance, and biological performance for biomedical applications. *Mat. Sci. Eng. C Mater. Biol. Appl.* 62, 634–642. doi: 10.1016/j.msec.2016.01.085

Kemnitz, E., Gross, U., Rudiger, S., and Shekar, C. S. (2003). Amorphous metal fluorides with extraordinary high surface areas. *Angew. Chem. Int. Ed.* 42, 4251–4254. doi: 10.1002/anie.200351278

Kickelbick, G. (2003). Concepts for the incorporation of inorganic building blocks into organic polymers on a nanoscale. *Prog. Polym. Sci.* 28, 83–114. doi: 10.1016/S0079-6700(02)00019-9

Laaksonen, P., Szilvay, G. R., and Linder, M. B. (2012). Genetic engineering in biomimetic composites. *Trends Biotechnol.* 30, 191–197. doi: 10.1016/j.tibtech.2012.01.001

Lai, C. Y., Hiltner, A., Baer, E., and Korley, L. T. (2012). Deformation of confined poly(ethylene oxide) in multilayer films. *ACS Appl. Mater. Interfaces* 4, 2218–2227. doi: 10.1021/am300240r

Liu, L.-Z., Hsiao, B. S., Ran, S., Fu, B. X., Toki, S., Zuo, F., et al. (2006). *In situ* WAXD study of structure changes during uniaxial deformation of ethylene-based semicrystalline ethylene–propylene copolymer. *Polymer* 47, 2884–2893. doi: 10.1016/j.polymer.2006.01.090

Logan, B. E., and Kilps, J. R. (1995). Fractal dimensions of aggregates formed in different fluid mechanical environments. *Water Res.* 29, 443–453. doi: 10.1016/0043-1354(94)00186-B

Mallick, B., Patel, T., Behera, R. C., Sarangi, S. N., Sahu, S. N., and Choudhury, R. K. (2006). Microstrain analysis of proton irradiated PET microfiber. *Nucl. Instrum. Methods Phys. Res. Sect. B Beam Interact. Mater. Atoms* 248, 305–310. doi: 10.1016/j.nimb.2006.04.153

Meyers, M. A., Chen, P.-Y., Lin, A. Y. M., and Seki, Y. (2008). Biological materials: Structure and mechanical properties. *Prog. Mater. Sci.* 53, 1–206. doi: 10.1016/j.pmatsci.2007.05.002

Munch, E., Launey, M. E., Alsem, D. H., Saiz, E., Tomsia, A. P., and Ritchie, R. O. (2008). Tough, bio-inspired hybrid materials. *Science* 322, 1516–1520. doi: 10.1126/science.1164865

Niemeyer, C. M. (2001). Nanoparticles, proteins, and nucleic acids: biotechnology meets materials science. *Angew. Chem. Int. Ed.* 40, 4128–4158. doi: 10.1002/1521-3773(20011119)40:22<4128::AID-ANIE4128>3.0.CO;2-S

Noack, J., Schmidt, L., Glasel, H. J., Bauer, M., and Kemnitz, E. (2011). Inorganic-organic nanocomposites based on sol-gel derived magnesium fluoride. *Nanoscale* 3, 4774–4779. doi: 10.1039/c1nr10843c

Palmer, L. C., Newcomb, C. J., Kaltz, S. R., Spoerke, E. D., and Stupp, S. I. (2008). Biomimetic systems for hydroxyapatite mineralization inspired by bone and enamel. *Chem. Rev.* 108, 4754–4783. doi: 10.1021/cr8004422

Peterlik, H., and Fratzl, P. (2006). Small-angle X-ray scattering to characterize nanostructures in inorganic and hybrid materials chemistry. *Monatsh. Chem.* 137, 529–543. doi: 10.1007/s00706-006-0462-8

Petermann, J., and Ebener, H. (1999). On the micromechanisms of plastic deformation in semicrystalline polymers. *J. Macromol. Sci. Phys. B.* 38, 837–846. doi: 10.1080/00222349908248142

Rawlings, R. D., Alexander, J. M., Anderson, J. C., and Leaver, K. D. (2013). *Materials Science.* Springer.

Samsoninkova, V., Seidt, B., Hanßke, F., Wagermaier, W., and Börner, H. G. (2017). Peptide–polymer conjugates for bioinspired compatibilization of internal composite interfaces: via specific interactions toward stiffer and tougher materials. *Adv. Mater. Interfaces* 4. doi: 10.1002/admi.201600501

Samsoninkova, V., Venkatareddy, N. L., Wagermaier, W., Dallmann, A., and Borner, H. G. (2018). Precision compatibilizers for composites: in-between self-aggregation, surfaces recognition and interface stabilization. *Soft Matter* 14, 1992–1995. doi: 10.1039/C7SM02518A

Schmidt, P. (1991). Small-angle scattering studies of disordered, porous and fractal systems. *J. Appl. Crystallogr.* 24, 414–435. doi: 10.1107/S0021889891003400

Silberschmidt, V. V., and Matveenko, V. P. (2015). *Mechanics of Advanced Materials, Vol. 199*. Springer International Publishing.

Sommerdijk, N. A., and de With, G. (2008). Biomimetic CaCO3 mineralization using designer molecules and interfaces. *Chem. Rev.* 108, 4499–4550. doi: 10.1021/cr078259o

Studart, A. R. (2012). Towards high-performance bioinspired composites. *Adv. Mater.* 24, 5024–5044. doi: 10.1002/adma.201201471

Wang, E., Lee, S.-H., and Lee, S.-W. (2011). Elastin-like polypeptide based hydroxyapatite bionanocomposites. *Biomacromolecules* 12, 672–680. doi: 10.1021/bm101322m

Wegst, U. G. K., Bai, H., Saiz, E., Tomsia, A. P., and Ritchie, R. O. (2015). Bioinspired structural materials. *Nat Mater.* 14, 23–36. doi: 10.1038/nmat4089

Zhu, L., Cheng, S. Z. D., Calhoun, B. H., Ge, Q., Quirk, R. P., Thomas, E. L., et al. (2000). Crystallization temperature-dependent crystal orientations within nanoscale confined lamellae of a self-assembled crystalline-amorphous diblock copolymer. *J. Am. Chem. Soc.* 122, 5957–5967. doi: 10.1021/ja000275e

Conflict of Interest: The authors declare that the research was conducted in the absence of any commercial or financial relationships that could be construed as a potential conflict of interest.